Structural evolution of a Briançonnais cover nappe, the Caprauna-Armetta Unit (Ligurian Alps, Italy)

ALESSANDRO MENARDI-NOGUERA

Università di Pisa, Dipartimento di Scienze della Terra, Via S. Maria 53, 56100 Pisa, Italy

Abstract—The Caprauna-Armetta Unit (CAU) is a Briançonnais cover nappe emplaced on the external margin of the Ligurian Briançonnais Zone. A structural analysis of the nappe indicates that there are four superposed deformations (D_1-D_4). D_1 produced large recumbent isoclinal folds associated with a strong axial-plane cleavage and a SW-trending lineation. These folds can be related to a SW-directed overthrust shear. D_2 produced open to moderately tight folds with subvertical axial planes, overturned towards the northeast. D_3 and D_4 are represented by large wavelength open folds affecting only the large-scale setting of the nappe.

A finite strain map of the nappe has been compiled using data from an oolitic limestone layer. The measured strains appears to be essentially the product of the D_1 phase. The measured ellipsoids are generally triaxial. The trend of the finite strain X axes is towards the southwest. Prolate ellipsoids with very high R_{xz} ratios occur on the inverted limbs and sometimes near the hinge zones of the anticlinal F_1 folds. Oblate ellipsoids are prevalent on the normal limbs. This pattern of finite strain resulted from deformation in a ductile shear zone generated within the tectonic units trailed at the base of the huge Helminthoid Flysch Nappe during its motion towards the foreland.

INTRODUCTION

THEORETICAL models of strain distribution in nappes and thrust sheets suggest that knowledge of the finite strain field may be useful for investigating the strain history and in formulating a model of nappe generation. Since the generation of nappes and thrust sheets is part of the mountain-building process, strain analysis of this class of structures goes beyond the simple description of local geological situations.

In the Ligurian Alps, within the Briançonnais Zone (Figs. 1 and 2), a small cover nappe exists with exceptionally well preserved and exposed structures that are probably related to nappe emplacement. This nappe, the Caprauna-Armetta Unit (CAU), is characterized by km-scale isoclinal recumbent folds associated with an axial-plane cleavage subparallel to the nappe boundaries. These structures are only slightly modified by the post-nappe deformational phases which affected all the Briançonnais tectonic units.

The thrust surfaces bounding the CAU delimit a volume that seems approximately lenticular in shape. In fact, a sole thrust and roof thrust converge along the south and northeast borders of the unit. Towards the southeast the CAU is limited by a normal fault that prevents direct observation, but in the Monte Carmo region the absence of the CAU in the nappe pile proves that the sole thrust and the roof thrust also converge in this direction. Towards the west the geometry of the thrust surfaces is unknown because the upper tectonic units are eroded.

The CAU and the units immediately above and below have undergone only anchimetamorphism or very low grade greenschist metamorphism (Messiga *et al.* 1982). The stratigraphic sequence of the CAU according to Fierro & Vanossi (1965) is summarized in Fig. 3. For an up-to-date synthesis on the regional geology with exhaustive references, the interested reader is referred to Vanossi *et al.* (1984).

DEFORMATION HISTORY

In the CAU four superimposed generations of structures have been recognized (D_1-D_4). The identification and classification of these structures have been carried out using overprinting criteria. Because of clear outcrops the structures of the different phases could be correlated according to the principle of continuity (Williams 1985). The attribution of the mesoscopic structures to higher order structures has been performed in a straightforward way by mapping the whole CAU at the 1 : 5000 scale. The mapping is shown in a very simplified form in Fig. 4. Some of the orientation data are summarized on equal area plots (Fig. 5).

D_1 *structures*

The fundamental D_1 structures are represented by non-cylindrical isoclinal recumbent folds (Fig. 6). An axial-plane cleavage (S_1) is associated with these folds (F_1). It appears more or less markedly penetrative depending on the lithology. Cross-cutting relationships between the S_1 cleavage and the bedding planes can be observed only in the hinge zones of the F_1 folds, at the interface between rocks with high competence contrast. In these situations S_1 does not intersect any pre-existent tectonic planar fabric.

An L_1 stretching lineation is locally present on the S_1 plane. This lineation is caused by the alignment of intraclasts and of conglomerate components (Fig. 7c). On the stereonet the L_1 lineation is strictly clustered around an axis directed towards 219° (Fig. 5).
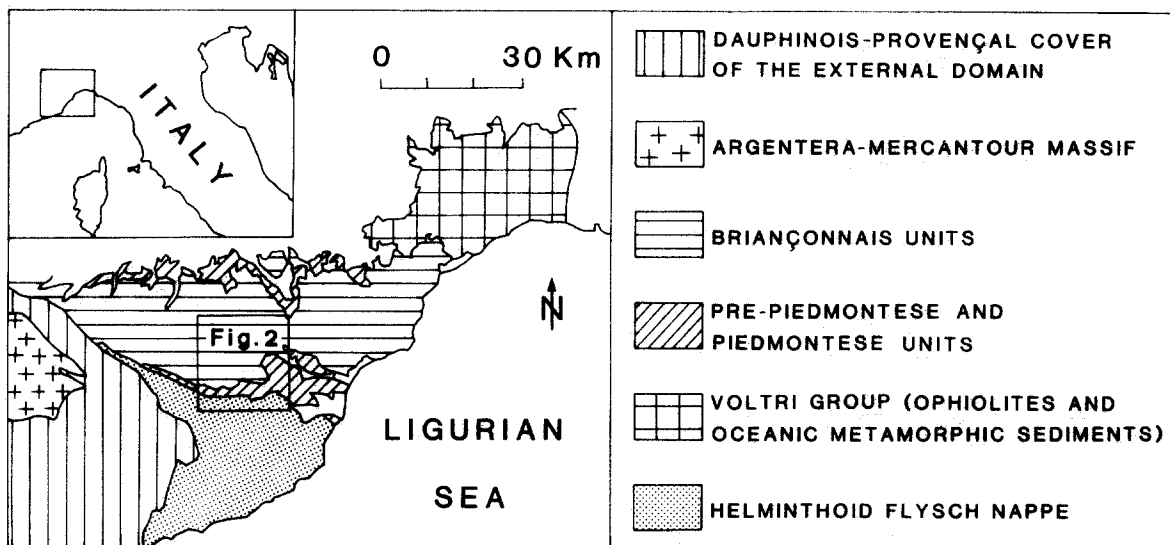
Fig. 1. Location of the Monte Armetta region in the geological setting of the Ligurian-Maritime Alps.

The F_1 folds form a coherent polyharmonic system well developed on the 1–1000 m scale. Mesoscopic F_1 folds are common in the thinly layered Cretaceous–Eocene calcareous schists. In the Eocene sandstones and limestones, F_1 folds with transposed hinges are emphasized by selective erosion (Fig. 7a). Cuspate F_1 folds can be observed at lithologic contacts between rocks with high competence contrast. On the stereonet (Fig. 5) the axes of the mesoscopic F_1 folds are rather scattered in the S_1 plane, but a clearly defined cluster is present at 120°. Rare well-developed sheath folds can be seen in the strongly deformed Cretaceous marly limestones (Fig. 7b). The best examples, found inside the inverted limbs of the largest F_1 folds, have an eye-like section normal to the L_1 lineation.

The asymmetry of the mesoscopic F_1 folds reflects their geometric position as parasitic folds on the limbs of 100–1000 m-scale isoclinal folds. These folds produce a partial or complete doubling of the stratigraphical sequence. Their enveloping surface and sense of vergence defines the hinge zones of km-scale recumbent isoclinal anticlinal folds separated by very narrow synclinal zones (Fig. 6). Some have been mapped in a continuous way across the CAU. These folds represent the most prominent structures of the nappe. The best exposures are on the eastern slopes of Monto Pesauto and the western slope of Monte Armetta (Fig. 6, sections A–C). Their axial planes are overturned towards the SW and thus consistent with the apparent regional direction of nappe transport. In the western sector of the CAU,
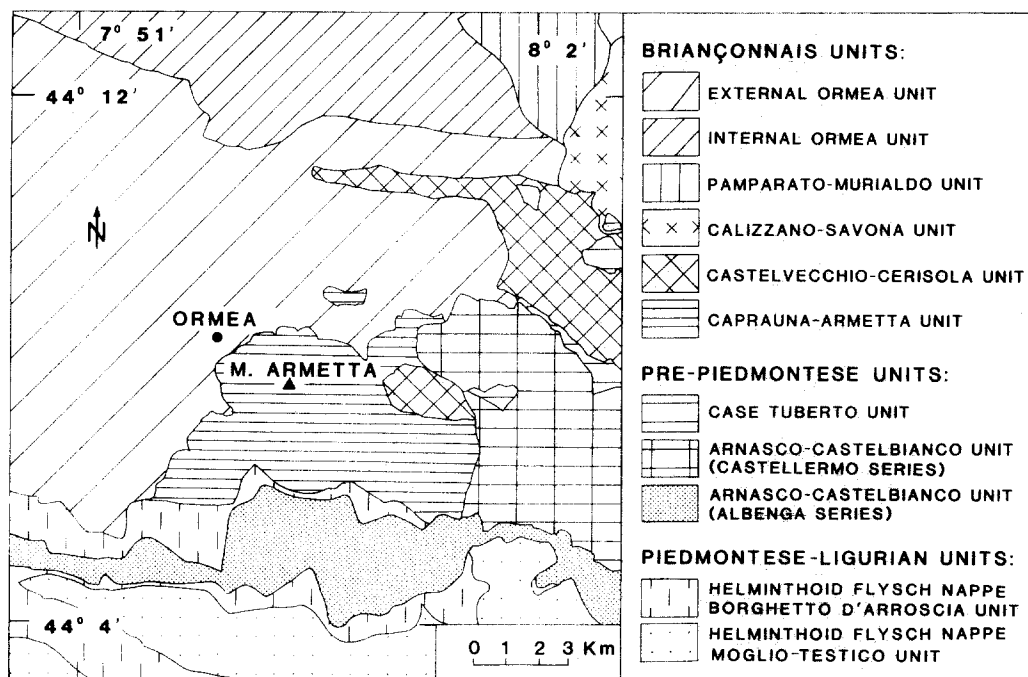

Fig. 2. Structural sketch map of the Monte Armetta region (Vanossi *et al.* 1984).
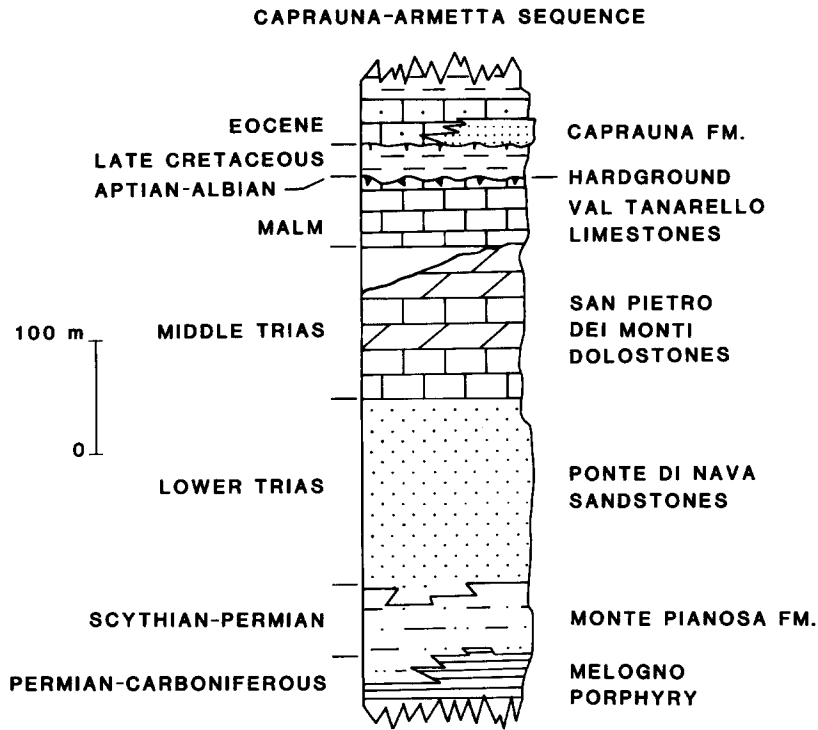
CAPRAUNA-ARMETTA SEQUENCE

Fig. 3. The stratigraphical sequence of the CAU according to Fierro & Vanossi (1965).

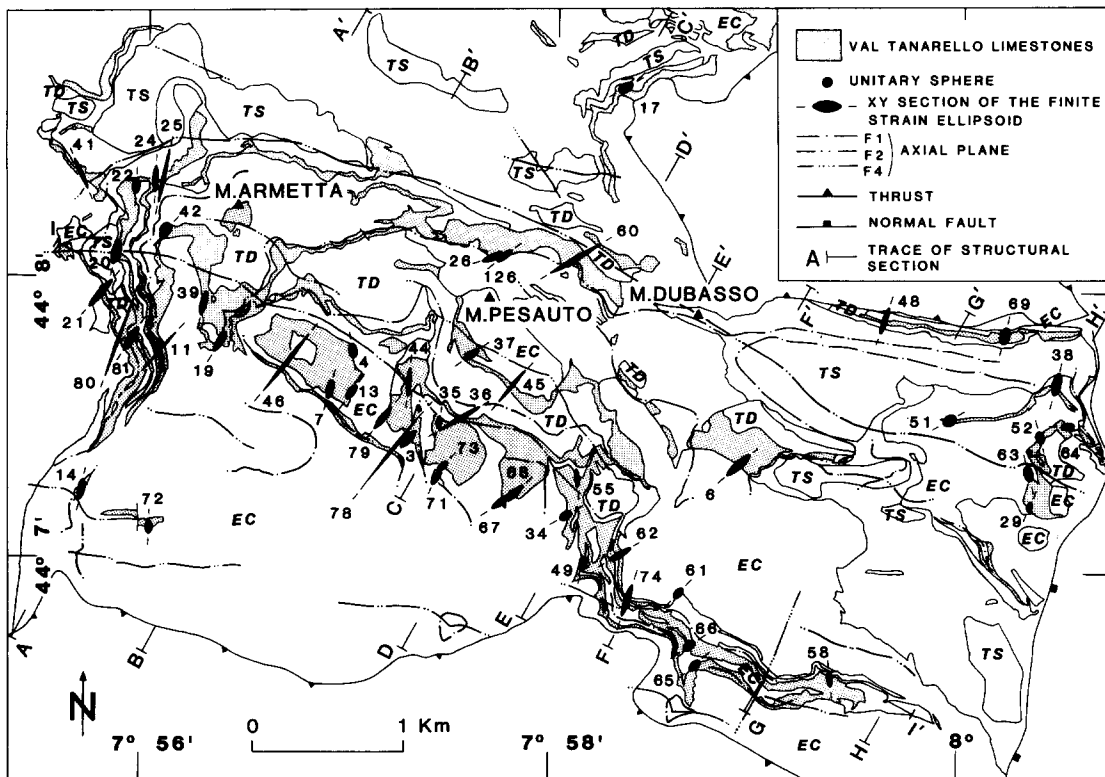Fig. 4. Structural and strain map of the CAU. The map is simplified and partly interpolated. TS: Melogno Porphyry (Permian–Carboniferous), Monte Pianosa Formation (Permian–Trias), and Ponte di Nava Quartz Sandstones (Lower Trias). TD: San Pietro dei Monti Dolostones (Middle Trias). EC: Caprauna Formation (late Cretaceous–Eocene). The X directions of the strain ellipsoid are marked with bars, the numbers refer to the sampling sites.

SO BEDDING

N

n=699

N

n=59

F1 FOLD AXES

S1 CLEAVAGE

N

n=1264

N

n=127

L1 LINEATION

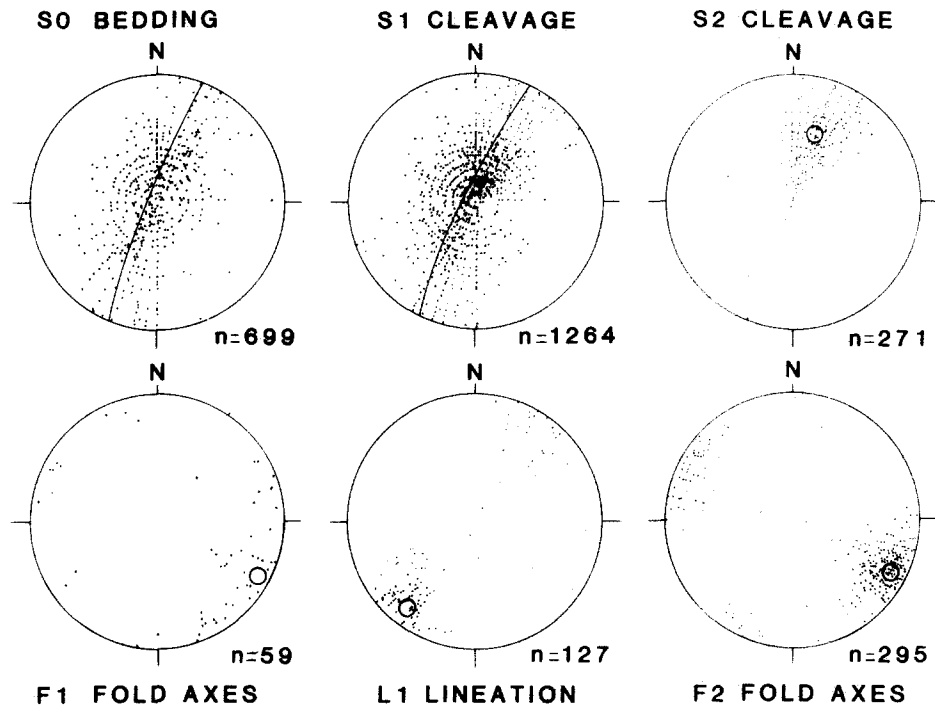**S2 CLEAVAGE**

N

n=271

N

n=295

F2 FOLD AXES

Fig. 5. Orientation data of planar and linear tectonic elements in the CAU (equal area, lower hemisphere; poles on equatorial circle are plotted once). Number of measurements (n) is indicated. Best-fit poles (open circles) in clusters or best-fit cyclographic traces in girdle distributions are shown.

SW   NE

A   M. ARMETTA   A'

1700   1700

1300   1300

B   B'

1300

1100   1100

M. PESAUTO   C'

1300

1100   1100

D'

D

1300

1100   M. DUBASSO   1100

E'

1300

S1 [   ]   1

S1 [S2]   2

1000 E   F'

1300

[   ]   3

SO [   ]   4

F   G'

SO [   ]   5

800   1000

S1 [   ]   6

G

700   S1 [   ]   7

H   H'

8

700   700
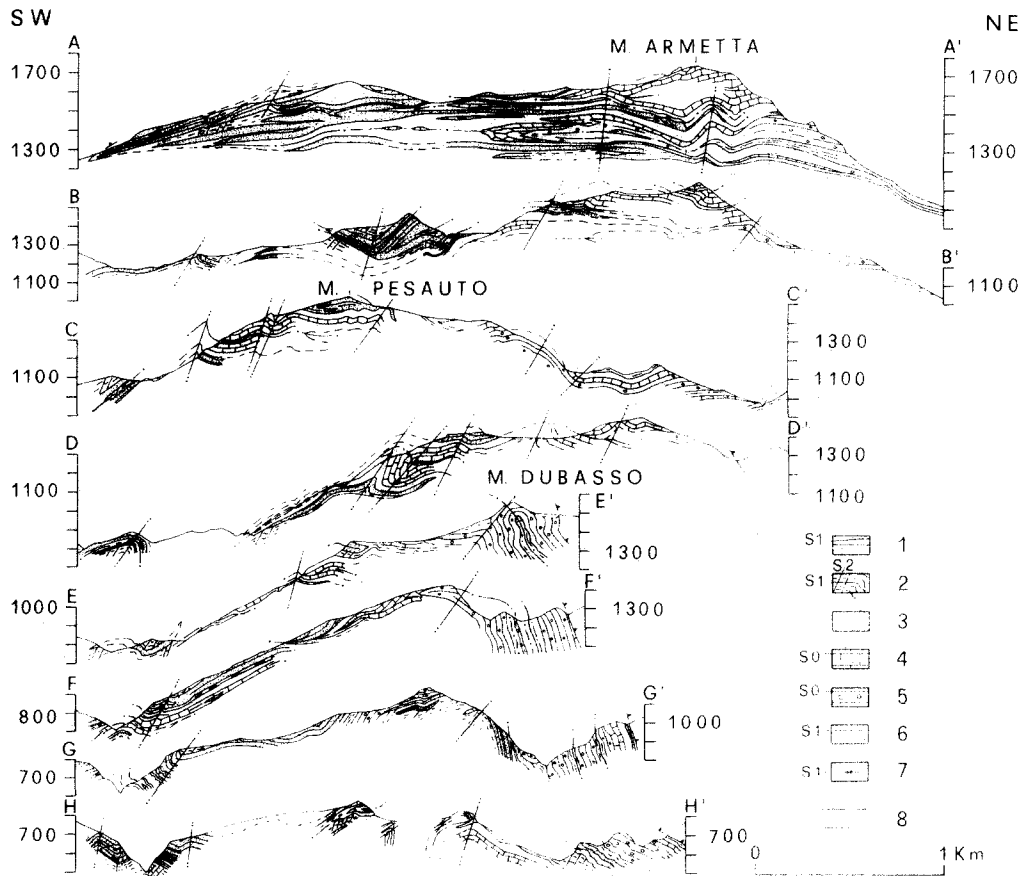   0   1 Km

Fig. 6. Structural sections across the CAU. Section traces are shown in Fig. 4. (1) Caprauna Formation (Eocene), arenaceous limestones. (2) Caprauna Formation (late Cretaceous–Eocene), pelitic–calcareous schist. (3) Val Tanarello Limestones (Malm). (4) San Pietro dei Monti Dolostones (Anisian–Ladinian). (5) Ponte di Nava Sandstones (Scythian). (6) Monte Pianosa Formation (Permian–Trias). (7) Melogno Porphyry (Permian–Carboniferous). (8) Traces of major F_1 and F_2 folds; number of dots refers to fold generations. S_0 is bedding. S_1 and S_2 are cleavages, respectively, associated with F_1 and F_2 folds.
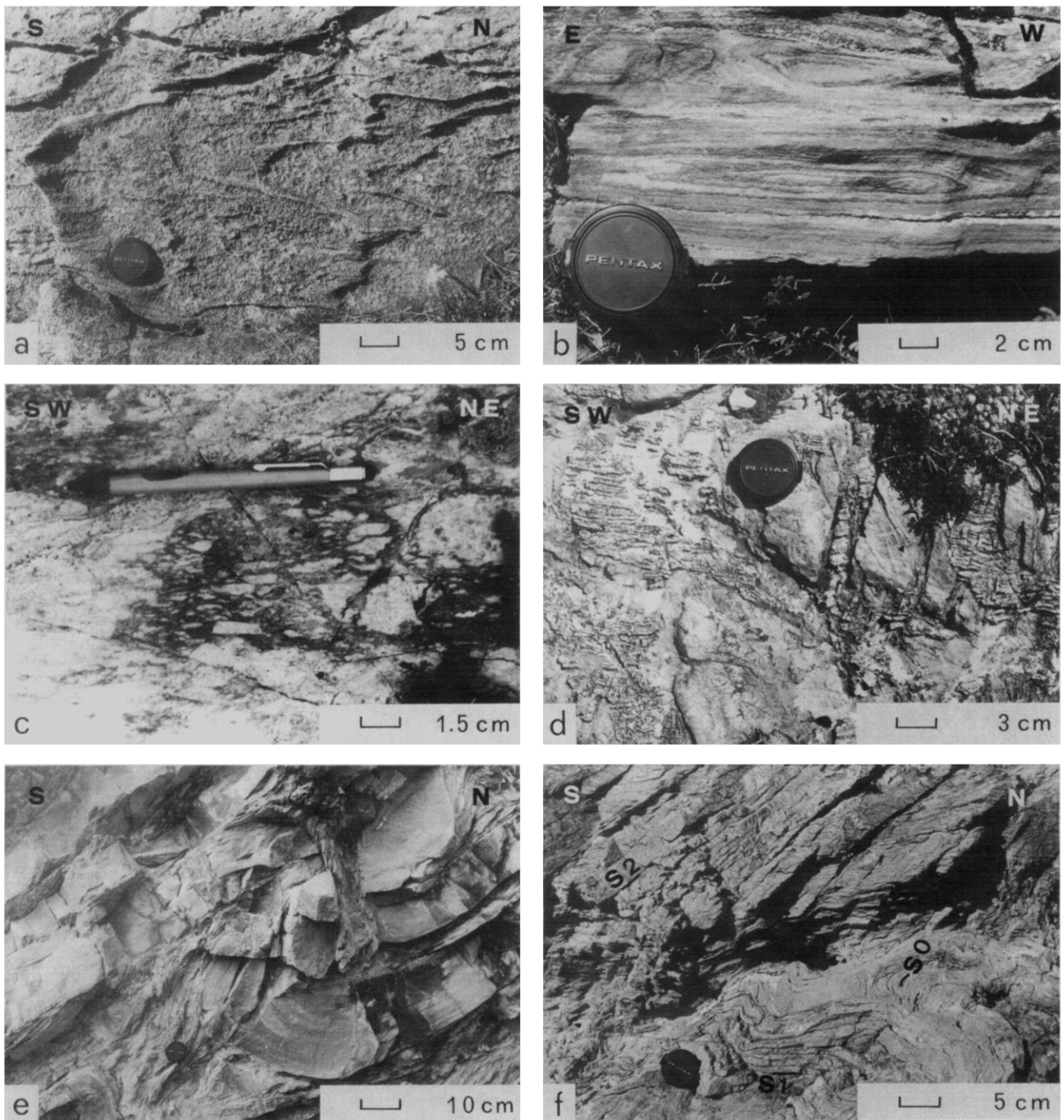
Fig. 7. (a) F_1 transposed fold hinge looking SW; arenaceous nummulitic limestone, Caprauna Formation. (b) Eye sections of sheath folds; marly limestone, Caprauna Formation. (c) Stretched intraclasts on the S_1 plane; Val Tanarello Limestones. (d) Rigid boudinage of the phosphatic–haematitic crust of the Aptian–Albian hardground, on the normal limb of the Monte Pesauto F_1 anticlinal fold; the open fractures are filled with calcite–quartz composite fibers trending 150°. (e) F_2 buckle fold looking SW in alternating pelitic and arenaceous rocks; Caprauna Formation. (f) Macroscopic superimposed cleavages. The well developed, SW-dipping, S_2 cleavage present in the pelitic schists die out in the more arenaceous ones; Caprauna Formation.
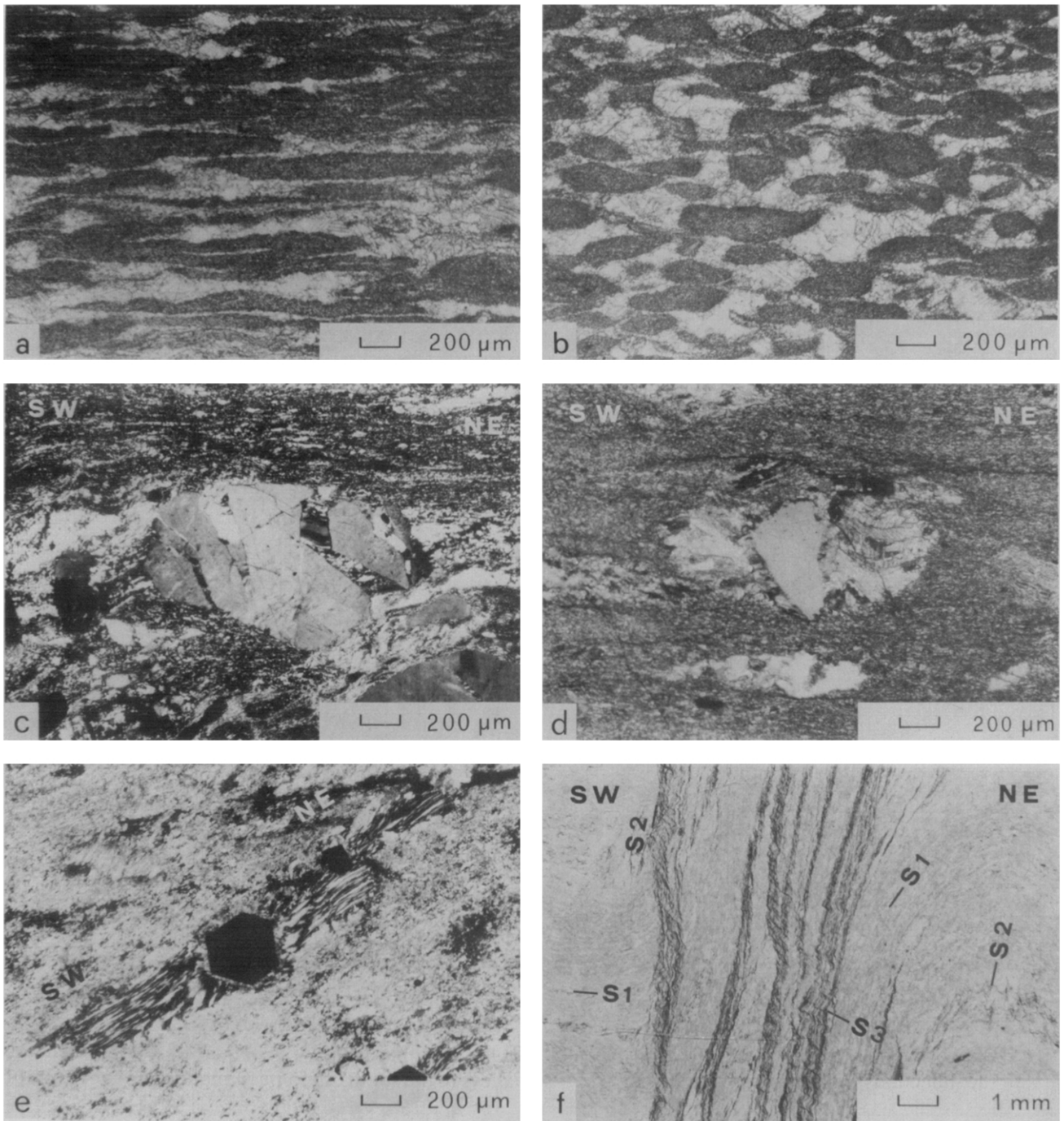
Fig. 9. (a) Deformed oolitic grainstone from site AR3, hinge zone of the anticlinal F_1 fold near the base of Monte Pesauto. The section is nearly parallel to the XZ plane of the strain ellipsoid; the strain ratio in the section is 10:14. (b) Sample AR3 cut in a plane nearly parallel to the YZ plane; strain ratio = 3.2. (c) Fragmented feldspar grain with quartz fibers filling the gaps; the section is perpendicular to S_1 and parallel to L_1. Monte Pianosa Formation, sampling site near the axial plane of the F_1 anticlinal fold of Monte Dubasso. (d) Composite calcite–quartz fibers around a quartz grain in the Val Tanarello Limestones, from the normal limb of the Monte Pesauto F_1 anticlinal fold. The section is normal to S_1 and parallel to L_1. The sense of shear expressed by the fibers is towards the SW. (e) Composite quartz–calcite fibers around a diagenetic pyrite crystal; marly limestones of the Caprauna Formation. The section is parallel to S_1. The sampling site is on the normal limb of the Monte Pesauto F_1 anticlinal fold. The quartz fibers record a sequence of NE-directed elongation increments followed by a final ENE directed extension. (f) Microcrenulation of S_1 and S_2 cleavages and development of a badly defined microscopic NE-dipping cleavage (S_3). Calcareous–pelitic schist, Caprauna formation.
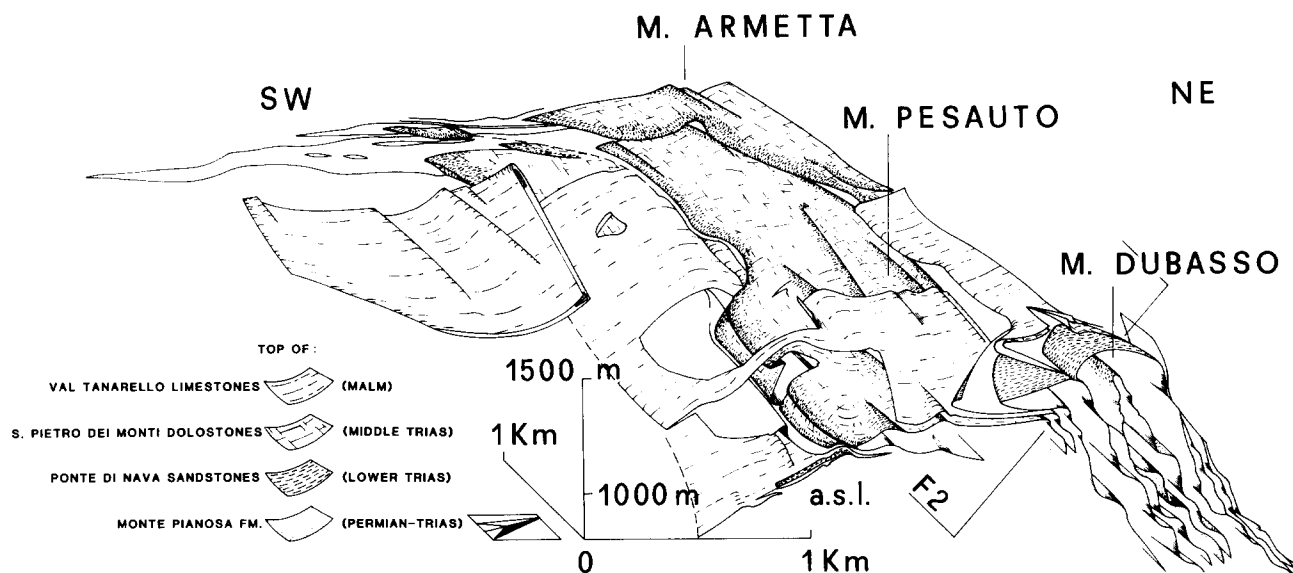
Fig. 8. Block diagram of the volume between profiles A and E of Fig. 6. The hinge lines of F_1 folds are strongly curved. Note the bifurcations of the hinge lines of Monte Pesauto and Monte Dubasso. Monte Armetta F_1 anticlinal folds. The general orientation of these folds is 120°. The F_2 and F_1 folds are broadly coaxial. The axial plane of the first-order F_2 Monte Dubasso antiform is shown.

their inverted limbs are continuous for kilometers. In the eastern sector, disrupted inverted limbs and isolated limbs appear (Fig. 6, sections G and H). The style of the 100 m-scale F_1 folds is clearly dependent on lithology. Hinges are generally sharp in the Jurassic and Eocene limestones. Triassic dolomitic limestones and quartz sandstones form rounded hinges. Boudinage at the m-scale of the more dolomitic layers in the lithologic alternations of the San Pietro dei Monti Dolostones is common on the limbs of the F_1 folds.

According to the geometry of the enveloping surfaces of the largest F_1 folds these can be attributed to Ramsay's (1967) Class 3, characterized by thickened hinges and thinned limbs (Fig. 6, section A). The parasitic folds in the hinge zones of the largest F_1 folds indicate a remarkable thickening of the Jurassic–Eocene portion of the deformed stratigraphic sequence, and lead to the accumulation of the younger formations at the nappe front. The Monte Dubasso and Monte Pesauto anticlinal folds (Fig. 8) are characterized by spectacular bifurcations of the hinges. The reconstructed F_1 axial planes (Fig. 8) show that the axes of the F_1 folds are locally curved; the inflections can measure up to 90°.

D_2 structures

The mesoscopic F_2 folds have straight limbs and an interlimb angle between 45 and 100° (Fig. 7e). The axial planes are subvertical or dip NE. These folds are strongly asymmetric. On the stereonet their axes are clustered around a maximum at 120–300°. Alternations of Ramsay's (1967) Class 1c and Class 3 folds can be observed in the Cretaceous–Eocene calcareous schists. The size of the F_2 folds ranges from the cm- to the km-scale. They are non-cylindrical, as is shown by significant variations in amplitude along their axes: the

F_2 amplitude decreases from SE to NW. The largest of the F_2 folds is a plurikilometric antiform well exposed on the eastern slope of Monte Dubasso (Fig. 4; Fig. 6, sections E–H). In the east sector of the CAU, the short limb of this antiform rotates the entire unit and the thrust surfaces of the overlying nappes into the vertical. This fact demonstrate that the D_2 phase can be dated as post-nappe emplacement.

A crenulation cleavage (S_2) is associated with the F_2 folds; it is developed and accompanied by transposition effects only in the most pelitic rocks (Fig. 7f). The S_2 strike is fairly constant in the whole nappe, plunging towards SW with a 40° mean dip (Fig. 2). The scattering in dip values is essentially due to the existence of convergent cleavage fans associated with the largest F_2 folds (Fig. 6, sections G and H).

The superposition of F_2 on F_1 folds has generated Ramsay's (1967) type 3 interference pattern, variety G as defined by Thiessen & Means (1980). The typical hook pattern, developed by this interference system on the surfaces normal to the axial planes, is visible at every scale. It is particularly clear in the NE–SE-trending valleys to the south of Monte Armetta. The continuity of this interference pattern in the CAU structural units implies that the angular relationship between the F_1 and F_2 folds is nearly constant and that these fold systems are approximately coaxial. Thus the F_2 folds should not produce significant rotations of the F_1 fold axes. The F_2 folds deform the L_1 lineation so that these scatter on a great circle whose pole coincides with the mean direction of F_2 fold axes (Fig. 5). The L_1 lineation and the D_2 compression direction must have been subparallel. The F_2 folds have, therefore, only affected the plunge values of L_1. The dispersion due to the component of tangential longitudinal strain during F_2 development was probably minor, as suggested by the great radius of curvature of the folds.
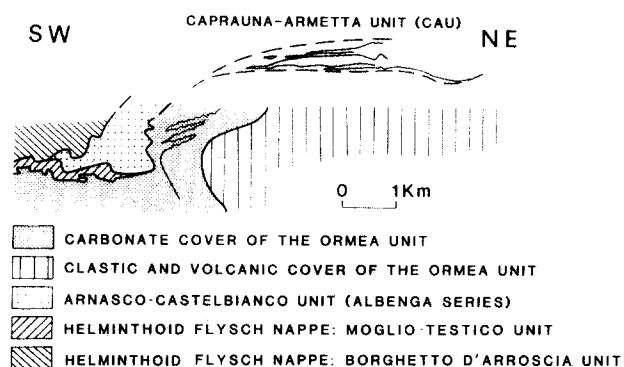
Fig. 10. Schematic regional section. The structures of the CAU are projected using section A (Fig. 6). The structures of the other units are redrawn from Vanossi *et al.* (1984). In this profile the evidence for the F_2 folds is minimal. The structures of the Ormea Unit are inspired from the well known Ponte di Nava vertical section. The CAU seems to be part of the normal limb of the large S-verging open fold exposed in this section.

D_3 structures

The F_3 structures are open mesoscopic folds in the S_2 cleavage. Their axial planes generally dip NE. The F_3 axes, rarely measurable, are directed towards 120–130°. F_3 folds are rather rare; they are present only in the most pelitic rocks. These folds lack a macroscopically evident axial-plane cleavage. In thin section, the mica-rich and calcite-rich domains of the S_1 and S_2 mineralogically differentiated crenulation cleavages are intersected by a very weak planar fabric, dipping NE (Fig. 9f). Relations between the F_3 mesoscopic folds and larger structures are not clear. The F_3 folds and a microcrenulation of the S_1 and S_2 cleavages may be the very weak effect of the deformation associated with the horizontal limb of the huge open fold which constitutes the front of the Ormea Unit (Fig. 10).

D_4 structures

The D_4 structures are folds (F_4) with a very large radius of curvature. They determine axial inflections at the regional-scale of the main post-nappe structures. The axial plunge of the F_1 and F_2 fold systems and the 20° dip of the whole CAU towards SE are due to the existence of these inflections. Inside the SE sector of the CAU a large F_4 antiform is present. Its limbs are gently inclined, the strike of its vertical axial plane is N–S. A regularly spaced family of joints, with N–S strike, is associated with the structural culmination of the antiform. The joints clearly intersect the D_2 structures. The antiform terminates northwards just where the hypothetical prolongation of its axial plane would cross the hinge of the large Monte Dubasso F_2 fold (Fig. 4). Another F_4 antiform is present north of Monte Pesauto. This structure does not seem to continue to the south, beyond the Monte Dubasso F_2 fold (Fig. 4).

The F_4 fold system can be studied only at regional-scale; the superposition of these folds on the older structures has generated a dome and basin interference

pattern that controls the cartographic distribution of the main tectonic units in the Ligurian Alps (Menardi-Noguera 1984a).

STRAIN ANALYSIS

The only strain markers that can be found in the stratigraphic sequence of the CAU (Fig. 3) nappe are ooids in a thin level of grainstone–packstone (Fig. 9a & b) at the top of the Val Tanarello Limestones. Sometimes, in the Aptian–Albian hardground, it is possible to observe phosphatized oolitic intraclasts that behaved as rigid inclusions during D_1. These intraclasts, preserved from deformation thanks to the competence contrast, show that the original ooids had small nuclei and low ellipticity. Study of the less deformed samples eliminates the possibility of diagenetic deformation due to compaction during the burial history (Menardi-Noguera 1984b). The competence contrast between ooids and micritic or sparry matrix should be very small; the lithologic uniformity of the oolitic layer also excludes lateral variations in competence contrast.

The strain was measured on three surfaces of oriented samples cut normal to the S_1 cleavage; two at 90°, the third at 45°. This choice was compelled by the brittleness of the samples. The deformed ooids were measured directly under the microscope by regular scanning of the three thin sections. The number of strain markers measured on each section ranges from 50–75 to 150 depending on the sample quality. The two-dimensional finite strain on the three surfaces has been calculated with the computer program developed by Peach & Lisle (1979), based on the θ-curve method (Lisle 1977a), a variant of the R-ϕ method developed by Ramsay (1967) and Dunnet (1969).

If the ellipticity of deformed ooids was too high to allow an accurate measure of ϕ, the two-dimensional strain was evaluated using the harmonic mean method (Lisle 1977b). The two-dimensional strain measurements have been combined to calculate the finite strain ellipsoids using the method and computer program described and developed by Owens (1984). A total of 53 finite strain ellipsoids were measured (Table 1).

SYNTECTONIC FIBERS

Syntectonic mineral fibers crystallized around rigid inclusions or inside fractures may be used as incremental strain markers (Ramsay & Huber 1983). Some good markers of this type have been found in the CAU. Unfortunately they are unevenly distributed throughout the structures so that a systematic quantitative study at the nappe-scale is problematic. In addition, all these markers are located along the normal limbs of the huge anticlinal F_1 folds. Nevertheless even a few fiber systems may provide valuable information about the deformation history that caused the observed finite strain field.

Calcite–quartz composite fibers are common inside

Table 1. Finite strain data from Val Tanarello Limestones in the CAU. Specimen locations are shown in Fig. 4. The ellipsoid axial ratios are normalized to constant volume ($XYZ = 1$). M: methods employed for the two-dimensional strain analysis; H: harmonic mean method; R: R/ϕ method. $k = \ln(X/Y)/\ln(Y/Z)$, $D = ((\ln X/Y)^2 + (\ln Y/Z)^2)$.

Site	M	$1 + e_1$	$1 + e_2$	$1 + e_3$	X AZ	X PL	Z AZ	Z PL	k	D
AR3	R	3.21	1.00	0.31	223	20	40	70	1.00	2.72
AR4	R	2.47	1.27	0.32	172	8	350	82	0.48	2.34
AR6	H + R	4.27	1.16	0.20	229	26	45	64	0.75	4.75
AR7	R	2.47	1.13	0.36	96	35	15	55	0.67	1.95
AR11	H	7.11	0.83	0.17	42	2	212	2	1.36	7.13
AR13	R	2.42	1.12	0.37	216	5	40	85	0.68	1.84
AR14	H + R	2.94	1.26	0.27	191	36	40	50	0.55	3.08
AR17	R	2.27	1.45	0.30	241	6	50	84	0.29	2.64
AR19	H	3.18	1.09	0.29	202	5	30	85	0.80	2.90
AR20	H + R	3.44	1.34	0.22	14	19	250	60	0.51	4.23
AR21	H + R	4.78	0.82	0.25	40	20	210	70	1.50	4.47
AR22	R	1.99	1.26	0.40	183	6	290	70	0.40	1.53
AR24	H	3.56	0.96	0.29	3	38	205	50	1.09	3.14
AR25	H + R	7.48	0.78	0.17	13	20	205	70	1.48	7.41
AR26	R	3.61	0.95	0.29	72	1	355	60	1.14	3.16
AR29	R	1.31	1.07	0.71	202	29	40	60	0.49	0.20
AR34	R	1.85	1.22	0.44	60	2	315	85	0.40	1.19
AR35	R	1.83	1.13	0.48	192	10	75	70	0.57	0.95
AR36	H	6.69	0.81	0.18	60	33	205	50	1.41	6.65
AR37	R	2.49	1.10	0.36	235	36	35	52	0.73	1.89
AR38	H + R	3.13	1.36	0.23	15	33	5	35	0.47	3.77
AR39	H + R	3.30	1.14	0.27	194	5	315	70	0.73	3.24
AR41	R	4.55	0.58	0.37	337	72	70	15	4.62	4.41
AR42	R	2.22	1.16	0.39	221	28	20	60	0.58	1.63
AR44	H + R	4.07	0.90	0.27	186	22	20	65	1.25	3.71
AR45	H + R	5.58	0.64	0.28	221	5	45	85	2.60	5.37
AR46	H + R	9.99	0.52	0.19	220	12	50	78	3.0	9.73
AR48	H + R	3.72	0.89	0.30	341	13	200	10	1.33	3.20
AR49	R	2.04	1.19	0.41	193	5	30	85	0.51	1.42
AR51	H	2.06	1.53	0.32	62	8	170	65	0.19	2.56
AR52	H + R	1.72	1.45	0.40	164	33	5	55	0.13	1.66
AR55	R	2.45	0.93	0.44	346	25	160	65	1.27	1.51
AR58	R	2.33	0.98	0.44	173	5	80	30	1.08	1.39
AR60	H + R	7.99	0.69	0.18	240	29	40	60	1.84	7.78
AR61	R	1.81	1.21	0.46	45	25	225	65	0.41	1.11
AR62	R	3.59	0.97	0.29	240	17	355	55	1.07	3.20
AR63	R	2.21	1.48	0.30	165	3	20	80	0.27	2.64
AR64	R	1.89	1.24	0.43	89	10	200	65	0.40	1.32
AR65	R	2.02	1.16	0.43	229	35	50	55	0.55	1.30
AR66	H + R	2.72	1.19	0.31	237	12	55	78	0.61	2.50
AR67	H + R	3.24	1.07	0.29	234	6	345	75	0.84	2.95
AR68	R	3.25	1.02	0.30	228	42	20	45	0.95	2.82
AR69	H	2.38	1.47	0.28	15	79	195	10	0.29	2.92
AR71	R	1.89	1.03	0.51	227	9	20	80	0.86	0.85
AR72	R	2.21	0.84	0.54	183	10	20	80	2.24	1.13
AR73	R	2.16	1.09	0.43	206	18	50	70	0.74	1.34
AR74	H + R	4.44	0.90	0.25	208	10	20	70	1.26	4.17
AR78	H + R	13.97	0.61	0.12	219	25	180	60	1.90	12.52
AR79	H + R	3.81	1.03	0.25	219	9	20	70	0.93	3.67
AR80	H + R	11.20	0.53	0.17	110	73	20	0	2.67	10.62
AR81	H + R	3.80	1.07	0.24	33	15	210	75	0.85	3.78
AR126	R	2.47	0.96	0.42	53	1	320	85	0.87	1.57

the mineralized part of the Aptian–Albian hardground. The fibers fill the gaps between boudins and have a diameter of 3 mm and are up to 15 cm long (Fig. 7d). These fiber systems are characterized by an overall NE–SW-directed growth. The fibers may show a very weak curvature in the growth plane, parallel to the S_1 cleavage. However their overall direction differs little from the L_1 direction measured in the limestones immediately under the hardground. Systems of quartz fibers subparallel to the L_1 macroscopic lineation can be observed in the Monte Pianosa Formation at the cores of the isoclinal F_1 folds of Monte Dubasso. The fibers are

crystallized as pressure shadows around clasts or inside fragmented quartz and feldspar clasts (Fig. 9c). Fibers underwent dynamic recrystallization, as shown by the presence of subgrains.

The deformation history recorded by these fiber systems is a sequence of non-coaxial extension increments with growth directions nearly parallel to the L_1 direction. This sequence could express a plane progressive simple shear strain. Asymmetry of recrystallized fibers and rigid body rotation of the clast fragments (Fig. 9c) is consistent with a SW-directed shear strain.

Quartz–calcite composite fibers are developed as pres-

sure shadows around isolated quartz clasts in the limestone filling of erosive hollows sealed by the phosphatic–haematitic crust of the Aptian–Albian hardground (Fig. 9d). These pressure shadows are made of syntaxial quartz fibers and of antitaxial calcite fibers. The calcite fibers are much more developed than the quartz ones; sometimes they are twinned or strongly recrystallized. Only the fibers conforming to the rigid fiber model (Ramsay & Huber 1983) have been studied. The growth direction of the fibers is entirely contained in the XZ plane of finite strain determined using deformed ooids, which shows that the part of the deformation history recorded by these fibers corresponded to plane strain. Solution phenomena at the grain borders that could indicate shortening in the Y direction have not been observed. All the studied pressure shadows record a non-coaxial deformation history constituted by a sequence of extension increments that could express a plane progressive simple shear strain towards the SE.

The calcareous schists occasionally contain well-developed pressure shadows made of antitaxial quartz and calcite fibers crystallized around euhedral crystals of pyrite. Because of the anisotropy indicated by the D_2 phase, the finite strain is generally heterogeneous at the sample-scale. A few outcrops of marly limestones attached to the Aptian–Albian hardground lack the S_2 cleavage, and offer a rare opportunity to study these pressure shadows in relation to the D_1 structures. On the S_1 plane the antitaxial quartz fibers record a sequence of almost coaxial extension increments directed towards the NE followed by a final extension increment directed towards the ENE (Fig. 9e). Thus the overall deformation history recorded by these pressure shadows is nearly plane strain with a weak extension in Y. From these data it is possible to draw some qualitative conclusions: the main part of the deformation history consists of a progressive simple shear strain; and the incremental extension direction shows only minor deviations from the NE–SW direction.

STRAIN VARIATION

The geometry and dimensions of the structures permit the assumption that the strain is homogeneous at the outcrop-scale in the Jurassic limestones. All finite strain measurements were made at the top of the Val Tanarello Limestones (Fig. 3). The strains were measured on a surface that in the unstrained state coincides with a single bedding surface. Therefore these values are comparable and give direct information on strain gradients inside the structures.

The D_2–D_4 phases do not modify the S_1 fabric in the Jurassic limestones since these limestones are never intersected by the S_2 cleavage. In fact, the X axes of the finite strain ellipsoid are subparallel to L_1 (Figs. 5 and 11). The D_2–D_4 phases have essentially affected the dip values of the long axes of the finite strain ellipsoids, and hence L_1. The S_1 and L_1 orientation data therefore allow
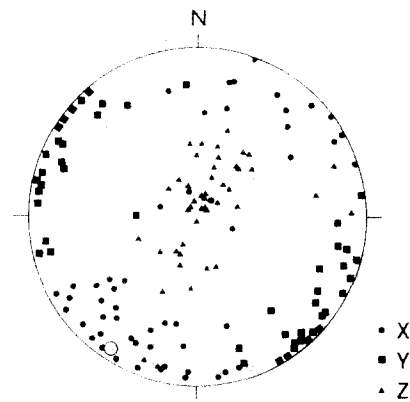

Fig. 11. Orientation of X, Y, Z, directions of the calculated finite strain ellipsoids (equal area lower emisphere). Open circle: best-fit pole of the X distribution.

reconstruction of the finite strain trajectories of the D_1 phase (Fig. 12).

The ooid strain values have been plotted on the Flinn logarithmic diagram (Fig. 13). They lie generally in the field of apparent flattening strain ($k < 1$). Some values lie in the field of apparent constrictional strain ($k > 1$), but with k values close to 1. The volume reduction that affected the Jurassic limestones is not measurable, but the very low grade metamorphism and the scarcity of calcite-filled veins and of stylolites, suggest that there was no extensive volume loss during deformation. The diagenetic volume reduction due to porosity loss should not be over 25% (Menardi-Noguera 1984b). A maximum of 30% volume reduction could move only a few more samples into the field of true constrictional strain. Thus ellipsoids that express a true constrictional strain really exist. The range of k and D values (Table 1) is not completely representative in that it does not include the extreme values obliterated by recrystallization in the most laminated Jurassic limestones. However, the observed dispersion is a good heterogeneity index of the strain field. In fact, there are significant differences in strain values between contiguous sampling sites located at equivalent structural positions; for example, sites 26–126 and 60, 48 and 69, and 37 and 45 (Fig. 4). The remarkable thickness variations of the deformed stratigraphic sequence are in accordance with the observed strain gradient.

The strain ellipsoids are oblate along the normal limbs of the F_1 anticlinal folds, far from the hinges. They are slightly oblate or prolate near the hinges. They are strongly prolate along the inverted limbs or near the hinge inflections of F_1 folds. The observed strain distribution cannot be directly related to simplified folding models. An analogy exists between the strain profile of Fig. 14, section A, and the strain distribution that characterizes folds generated by buckling and later flattened (Ramsay 1967, Hobbs et al. 1976), or folds generated by simultaneous buckling and flattening (Hudleston & Stephansson 1973).

The generation of hinge-thickened Class 3 folds, such as those observed in the CAU, necessarily implies a
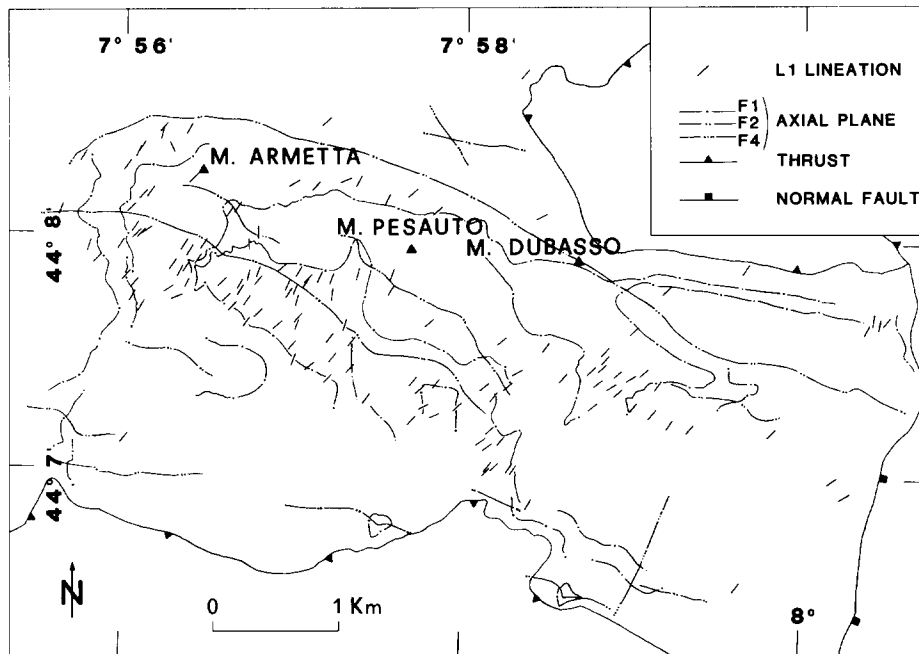
Fig. 12. Map of the L_1 lineation. Slight variations in orientation between adjacent domains suggest convergence and divergence of the X finite strain trajectories, probably arising from the general triaxial nature of the finite strain ellipsoid.

flattening of the folds (Ramsay 1967, Hudleston & Stephansson 1973, Parrish et al. 1976, Shimamoto & Hara 1976). On the other hand, the non-plane strain and the marked asymmetry of the F_1 folds show that it is necessary to consider more complex models of folding than the two-dimensional symmetric ones of the basic theory.

Very long thinned inverted limbs characterized by high X/Z strain ratios can originate only by localized simple shear acting on bedding planes inclined to the
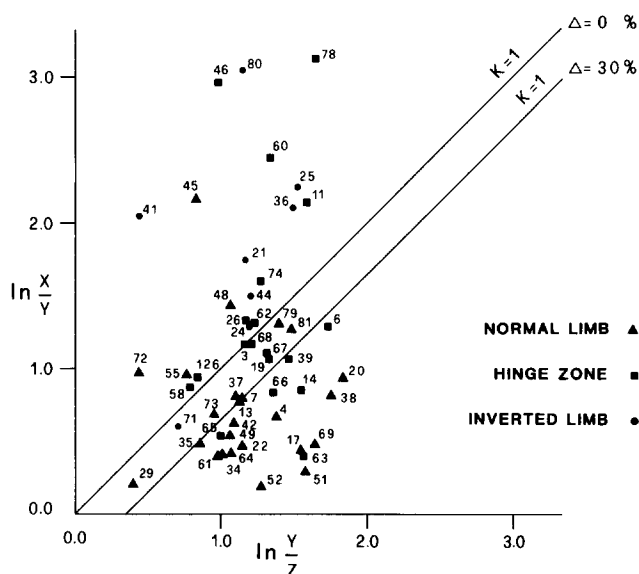

Fig. 13. Plot of finite strain values from 53 sites on Flinn's logarithmic diagram (Ramsay 1967). Lines that represent plane strain for no volume change and 30% volume decrease are represented. These lines separate the field of the true constrictional deformation (left) from the field of the true flattening deformation (right). The specimen numbers refer to Table 1.
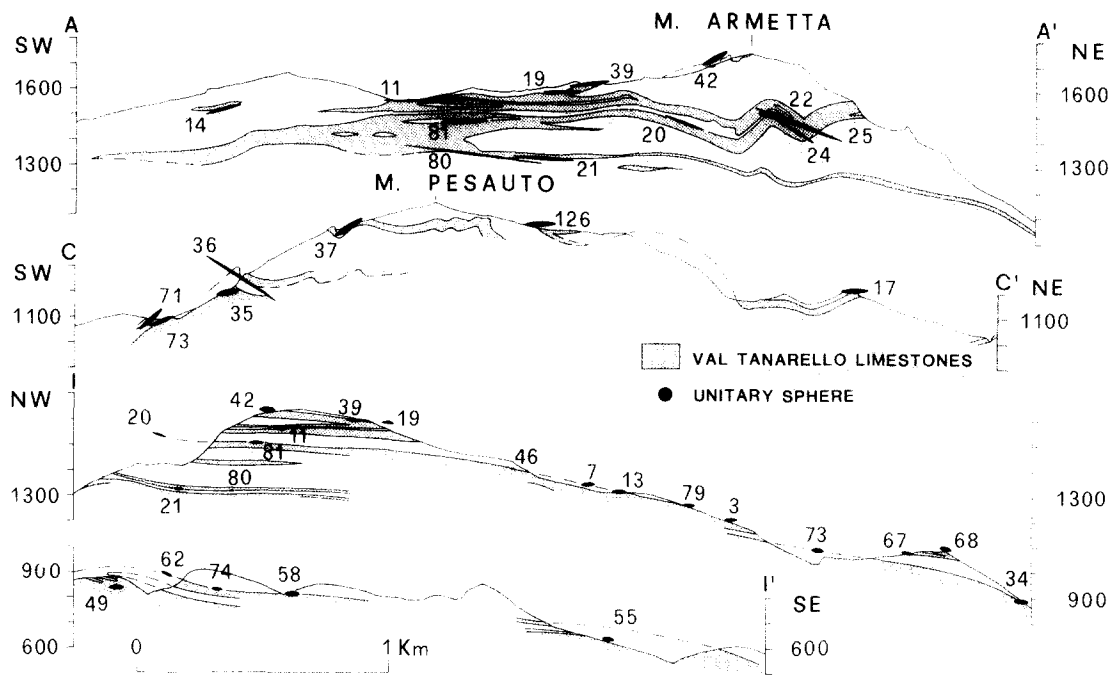
shear plane. Thinned inverted limbs and the asymmetric shape of the F_1 folds are features common to folds developed in simple shear regimes.

In the CAU multilayer sequence, the originally thickest and more competent layers are the Triassic dolomitic limestones and quartz sandstones. The rounded hinges characterizing the outer arc of these layers within some of the greatest F_1 folds denote an origin by buckling. The buckling theory predicts that a buckle fold starts to behave as a passive marker when the decreasing interlimb angle is less than 100°. But when the fold becomes passive it cannot deform by homogeneous strain if the competence contrast does not vanish (Ghosh 1974); as a consequence the late strain (respect to fold nucleation) must be lower in the competent layer that initiated the buckling than in the less competent ones. The strain pattern observed in the Jurassic limestones of the CAU, a comparatively not very competent layer, probably developed during the final stage of D_1 folding. The coexistence of oblate and prolate ellipsoids observed in the CAU is not exceptional and has been observed in many tectonic bodies (Hossack 1978, Siddans 1979, Coward & Kim 1981, Kligfield et al. 1981, Beach 1982, Williams et al. 1984, Platt & Behrmann 1986).

In the CAU, the shear strain localization suggested by the existence of thinned inverted limbs and the strain measurements may further contribute to the dispersion observed in the Flinn diagram (Fig. 13). A component of heterogeneous wrench shear could explain the presence of prolate ellipsoids located in inverted limbs and hinge zones of F_1 folds. This component could have arisen from differential transport of the nappe, caused by frictional drag along lateral ramps of the sole thrust.

The D_1 style of folding, and syntectonic mineral fibers,

Fig. 14. Strain sections. In section A the strain ellipsoid is characterized by high X/Z strain ratios in the inverted limbs and hinge zones of F_1 folds; lower values are observed in the normal limbs. In section I–I' (bottom), perpendicular to the L_1 direction, along the normal limbs of F_1 folds, the strain ellipsoid shows small variations in the $Y-Z$ ratio. Some corrections for small-scale F_2 mesoscopic folding have been introduced.

show that the D_1 structures have been developed in a tectonic environment characterized by an important component of progressive heterogeneous simple shear directed towards the SW, parallel to the regional direction of tectonic transport. The pattern of D_1 finite strain in the F_1 folds, which resembles in part those of folds developed by tangential longitudinal strain, is also characteristic of shear zones with non-parallel walls (Ramsay & Huber 1987). As shown by mapping, the thrust surfaces bounding the CAU are not parallel; the lenticular shape of the CAU resembles that of a horse.

The only tectonic unit overlying the CAU that appears to be regionally continuous is the Helminthoid Flysch Nappe. The very low degree of metamorphism of the CAU suggests that this nappe escaped the crustal underthrusting that affected the more internal Briançonnais units. Probably the sedimentary sequence forming the CAU was detached and incorporated at the base of the Helminthoid Flysch Nappe as the thrust systems propagated downwards.

The features of the CAU and the regional data allows the hypothesis that the most important part of the structural evolution of this Briançonnais Nappe occurred in a ductile shear zone generated within the internal Briançonnais units and Pre-Piedmontese units trailed at the base of the Helminthoid Flysch Nappe during its motion towards the SW.

TECTONIC SYNTHESIS

During the Eocene the Ligurian Briançonnais began to be affected by underthrusting along an intracontinen-

tal shear zone dipping towards the NE (Vanossi et al. 1984). Probably the CAU nucleated as a tectonic unit near the emergence of a major crustal shear plane when a younger thrust flat splayed off the footwall and ramped upsection to rejoin the upper thrust. Forming a horse structure, the CAU was expelled from this thrust, and was trailed along with other more internal units at the base of the Helminthoid Flysch Nappe. This nappe and the CAU were emplaced onto the external Briançonnais domain while the Briançonnais internal margin was undergoing HP–LT metamorphism.

The main part of the D_1 strain of the CAU accumulated in a shear zone created at the base of the nappe pile while it was in motion towards the foreland. The F_1 folds may have nucleated from internal unstabilities in the layered sequence undergoing shear deformation. The developing of a pervasive LS fabric, the amplification of F_1 folds, the thinning of their inverted limbs and the style of the F_1 folds were produced during this event.

After nappe emplacement, the CAU and the pile of nappes in which it is inserted were affected by the D_2 phase that generated NE-vergent asymmetric folds. The D_2 phase seems to be the product of the regionally recognized backfolding and backthrusting event, which has been related to the final stage of continental collision (Roeder 1980).

Late folding phases ($D_3–D_4$) determined the final setting of the CAU, now gently dipping towards the SE and outcropping at the eastern periclinal termination of a very large domal structure. The significance of these phases is under debate. According to Vanossi et al. (1984) D_3 could be the effect of the late thrusting of the Briançonnais nappe pile onto the Dauphinois Domain;

D_4 could be related to the development of the Ligurian orocline.

REFERENCES

Beach, A. 1982. Strain analysis in a cover thrust zone, external French Alps. *Tectonophysics* **88**, 333–346.

Coward, M. P. & Kim, J. H. 1981. Strain within thrust sheets. In: *Thrust and Nappe Tectonics* (edited by McClay, K. R. & Price, N. J.). *Spec. Publs geol. Soc. Lond.* **9**, 275–292.

Dunnet, D. 1969. A technique of finite strain analysis using elliptical particles. *Tectonophysics* **7**, 117–136.

Fierro, G. & Vanossi, M. 1965. Nuovi elementi per la stratigrafia del Brianzonese ligure tra il T. Corsaglia ed il T. Pennavaira. *Atti Ist. geol. Pavia* **16**, 17–35.

Ghosh, S. K. 1974. Strain distribution in superposed buckling folds and the problem of reorientation of early lineations. *Tectonophysics* **21**, 249–272.

Hobbs, B. E., Means, W. D. & Williams, P. F. 1976. *An Outline of Structural Geology.* Wiley, New York.

Hossack, J. R. 1978. The correction of stratigraphic sections for tectonic finite strain in the Bygdin area, Norway. *Q. Jl geol. Soc. Lond.* **135**, 229–241.

Hudleston, P. J. & Stephansson, O. 1973. Layer shortening and fold-shape development in the buckling of single layers. *Tectonophysics* **17**, 299–321.

Kligfield, R., Carmignani, L. & Owens, W. H. 1981. Strain analysis of a Northern Apennine shear zone using deformed marble breccias. *J. Struct. Geol.* **3**, 421–436.

Lisle, R. J. 1977a. Clastic grain shape and orientation in relation to cleavage from the Aberystwyth Grits, Wales. *Tectonophysics* **39**, 381–395.

Lisle, R. J. 1977b. Estimation of tectonic strain ratio from the mean shape of deformed elliptical markers. *Geologie Mijnb.* **56**, 140–144.

Menardi-Noguera, A. 1984a. Nuove osservazioni sulla struttura del massiccio del Monte Carmo (Alpi Liguri). *Boll. Soc. Geol. ital.* **103**, 189–203.

Menardi-Noguera, A. 1984b. Misure di strain finito nell Unità di Caprauna-Armetta (Alpi Liguri). *Mem. Soc. Geol. ital.* **28**, 537–547.

Messiga, B., Oxilia, M., Piccardo, G. B. & Vanossi, M. 1982. Fasi metamorfiche e deformative alpine nel Brianzonese e nel Pre-piemontese-Piemontese esterno delle Alpi Liguri: un possibile modello evolutivo. *Rc. Soc. miner. Petr. ital.* **38**, 261–280.

Owens, W. H. 1984. The calculation of the best fit ellipsoid from elliptical sections on arbitrarily orientated planes. *J. Struct. Geol.* **6**, 571–578.

Parrish, D. K., Krivz, A. L. & Carter, N. L. 1976. Finite-element folds of similar geometry. *Tectonophysics* **32**, 183–207.

Peach, C. J. & Lisle, R. J. 1979. A Fortran IV program for the analysis of tectonic strain using deformed elliptical markers. *Comput. Geo-Sci.* **5**, 325–334.

Platt, J. P. & Behrmann, J. H. 1986. Structures and fabrics in a crustal-scale shear zone, Betic Cordillera, SE Spain. *J. Struct. Geol.* **8**, 15–33.

Ramsay, J. G. 1967. *Folding and Fracturing of Rocks.* McGraw-Hill, New York.

Ramsay, J. G. & Huber, M. I. 1983. *The Techniques of Modern Structural Geology*—Vol. 1. *Strain Analysis.* Academic Press, London.

Ramsay, J. G. & Huber, M. I. 1987. *The Techniques of Modern Structural Geology*—Vol. 2. *Folds and Fractures.* Academic Press, London.

Roeder, D. 1980. Geodynamics of the Alpine–Mediterranean system—a synthesis. *Eclog. geol. Helv.* **73**, 353–377.

Shimamoto, T. & Hara, I. 1976. Geometry and strain distribution of single-layer folds. *Tectonophysics* **30**, 1–34.

Siddans, A. W. B. 1979. Deformation, metamorphism and texture development in Permian mudstones of Glarus Alps. *Eclog. geol. Helv.* **72**, 601–621.

Thiessen, R. L. & Means, W. D. 1980. Classification of fold interference patterns: a re-examination. *J. Struct. Geol.* **2**, 311–316.

Vanossi, M., Cortesogno, L., Galbiati, B., Messiga, B., Piccardo, G. & Vannucci, R. 1984. Geologia delle Alpi Liguri: dati, problemi, ipotesi. *Mem. Soc. Geol. ital.* **28**, 5–75.

Williams, P. F. 1985. Multiply deformed terrains—problems of correlation. *J. Struct. Geol.* **7**, 269–280.

Williams, G. D., Chapman, T. J. & Milton, N. J. 1984. Generation of finite strain patterns by progressive thrust faulting in the Laksefjord nappe, Finnmark. *Tectonophysics* **107**, 177–186.